ELSEVIER

Compositionally and structurally redesigned high-energy Ni-rich layered cathode for next-generation lithium batteries

Un-Hyuck Kim [1], Jae-Hyung Kim [1], Jang-Yeon Hwang [1], Hoon-Hee Ryu [1], Chong S. Yoon [2,*], Yang-Kook Sun [1,*]

[1] Department of Energy Engineering, Hanyang University, Seoul 04763, South Korea
[2] Department of Materials Science and Engineering, Hanyang University, Seoul 04763, South Korea

A hybrid cathode, $Li[Ni_{0.886}Co_{0.049}Mn_{0.050}Al_{0.015}]O_2$, consisting of a core of $Li[Ni_{0.934}Co_{0.043}Al_{0.015}]O_2$ encapsulated by $Li[Ni_{0.844}Co_{0.061}Mn_{0.080}Al_{0.015}]O_2$ is prepared. This core/shell-type structure combining a Ni-enriched $Li[Ni_xCo_yAl_{1-x-y}]O_2$ (NCA) cathode with an Al-doped $Li[Ni_xCo_yMn_{1-x-y}]O_2$ (NCM) cathode provides an exceptionally high discharge capacity of 225 mAh g^{-1} at 4.3 V and 236 mAh g^{-1} at 4.5 V. The hybrid cathode also exhibits microstructural attributes that are beneficial to long-term cycling stability, namely, spatially correlated peripheral primary particles that are crystallographically textured to expedite Li intercalation and nano-sized core primary particles retard the propagation of interparticle microcracks. In addition, ordered intermixing of Li and transition metal ions is observed in the cycled hybrid cathode. This cation ordering stabilizes the host structure during cycling and facilitates Li intercalation. These structural features allow the hybrid cathode to retain 91% of its initial capacity after 1000 cycles, which easily surpasses the performance of currently available cathodes.

Introduction

In recent years, lithium-ion batteries (LIBs) have become the main energy source for portable electronic devices and home appliances, electric vehicles (EVs), and energy storage systems because they have high gravimetric and volumetric energy densities and satisfy the thermal stability and battery life requirements [1–4]. Despite these successful applications, the current LIB technology still falls short of meeting the EV performance standard demanded for wide consumer appeal. The main drawbacks of LIBs, including cost and inadequate energy density, have caused the driving range of EVs to be substantially inferior to those of internal combustion engine vehicles (ICEVs). In order for LIB-powered EVs to become competitive against ICEVs, it is necessary to increase the energy density, lower the cost, and extend the lifetime of current LIBs [4–8]. The overall performance of a LIB is largely limited by its cathode, which has a lower capacity (e.g., 180 mAh g^{-1} for $Li[Ni_{0.6}Co_{0.2}Mn_{0.2}]O_2$) than the graphite anode (360 mAh g^{-1}). Furthermore, the cathode is the most expensive and also the heaviest among the main components of a LIB. Therefore, increasing the cathode energy density will make EV batteries cheaper and lighter. Although other types of cathode materials are available for LIBs, layered $Li[Ni_xCo_y(Al\ or\ Mn)_{1-x-y}]O_2$ (Al = NCA or Mn = NCM) materials have been the most commercially successful cathode materials for EVs, as evidenced by Tesla Motors adopting an NCA cathode, $Li[Ni_{0.8}Co_{0.15}Al_{0.05}]O_2$, in its Model S, which has a driving range of 270 miles [9]. To reach the required energy density for EVs (350 Wh kg^{-1} for the driving range threshold of 300 miles per charge), the Ni content in NCA or NCM cathodes has to be considerably more than $\times = 0.8$ to deliver a discharge capacity greater than 200 mAh g^{-1}. Although Ni enrichment ($x > 0.8$) will provide the needed extra capacity (e.g., ~220 mAh g^{-1} for $Li[Ni_{0.90}Co_{0.05}Mn_{0.05}]O_2$) [10,11], the battery life and thermal safety are typically compromised due to rapid capacity fading and the abundance of reactive Ni^{4+} species [10–15].

* Corresponding authors.
E-mail addresses: Yoon, C.S. (csyoon@hanyang.ac.kr), Sun, Y.-K. (yksun@hanyang.ac.kr).

https://doi.org/10.1016/j.mattod.2018.12.004

To overcome the inherent instability of Ni-rich NCM or NCA cathodes, a compositional gradation approach, which renders the particle core Ni-rich for high capacity and the surface Ni-deficient (or Mn-rich) for cycling and thermal stability, was introduced [16–20]. Although this approach is widely recognized as one of the most practical solutions proposed to date, it, becomes impractical at increasingly high Ni contents because the required concentration gradient at the particle periphery is excessively steep. In this report, we attempt to address the inherent structural instability of Ni-rich layered cathodes through a pluralistic approach by reengineering the composition gradation scheme to develop a hybrid NCA-NCM cathode. The proposed hybrid cathode, Li$[Ni_{0.886}Co_{0.049}Mn_{0.050}Al_{0.015}]O_2$, is composed of a Ni-rich NCA core of Li$[Ni_{0.934}Co_{0.043}Al_{0.015}]O_2$ encapsulated by a 1-μm-thick Al-doped NCM shell of Li$[Ni_{0.844}Co_{0.061}Mn_{0.080}Al_{0.015}]O_2$ (denoted as NCA-NCMA90 hereafter). The NCA-NCMA90 particle interior consists of a Ni-rich NCA cathode with a composition close to Li$[Ni_{0.8}Co_{0.15}Al_{0.05}]O_2$, which has been extensively field-tested [9,21,22], whereas the encapsulating Al-doped NCM layer provides a Mn-enriched surface, which has been proven to stabilize the surface chemistry and structure [23–25]. The stabilization of NCM cathodes by Al-doping has been demonstrated clearly by Al-doped Li$[Ni_{0.61}Co_{0.12}Mn_{0.27}]O_2$, as this cathode retains its initial capacity without a significant loss after 3000 cycles [26]. In addition, the proposed hybrid cathode necessarily contains concentration gradients in both Mn and Ni because of the relatively Ni-poor and Mn-rich surface compositions. These concentration gradients, confined to the NCMA encapsulating layer, produce spatially correlated particle packing and a radial crystallographic texture that have been the signature microstructural features of compositionally graded NCM cathodes. Moreover, cation ordering (ordered intermixing of Li and transition metal (TM) ions in both the Li and TM layer planes), which was first detected in Zr-doped $LiNiO_2$ and improved the cycle life of $LiNiO_2$ [27], was also observed during cycling of the NCA-NCMA90 cathode. The observed cation ordering is believed to be partially responsible for stabilizing the cathode surface and the remarkable long-term cycling stability demonstrated by the proposed hybrid cathode. To support and verify the experimental and characterization results for the NCA-NCMA90 cathode, the structural and electrochemical properties of the hybrid cathode were benchmarked against those of a conventional Ni-rich NCA cathode, Li$[Ni_{0.888}Co_{0.097}Al_{0.015}]O_2$ (denoted as NCA90 hereafter).

Materials and methods

Synthesis of cathode materials

Synthesis of NCA90 (Li$[Ni_{0.888}Co_{0.097}Al_{0.015}]O_2$)

The spherical NC $[Ni_{0.90}Co_{0.10}](OH)_2$ precursor was synthesized via the co-precipitation method using an aqueous solution of 2.0 M $NiSO_4{\cdot}6H_2O$ and $CoSO_4{\cdot}7H_2O$ (Ni:Co = 9:1, molar ratio) as the starting material. A homogeneously mixed solution was fed into a batch reactor (17 L) filled with a solution of deionized water, NH_4OH (aq), and NaOH under a replenished N_2 atmosphere. Concurrently, 4 M NaOH (aq) (molar ratio of NaOH to transition metal = 2.0) and an NH_4OH-chelating agent (aq) (molar ratio of NH_4OH to transitionmetal = 1.2) were pumped separately into the reactor. The final precursor powder was obtained through filtration, washing, and vacuum drying at 110 °C for 12 h. To obtain Li$[Ni_{0.888}Co_{0.097}Al_{0.015}]O_2$, the precursor, $[Ni_{0.90}Co_{0.10}](OH)_2$, was mixed with $LiOH{\cdot}H_2O$ and $Al(OH)_3{\cdot}3H_2O$ (Li:Al:(Ni + Co) = 1.01:0.015:0.985, molar ratio) and calcined at 730 °C for 10 h under an oxygen atmosphere.

Synthesis of NCA-NCMA90 (Li$[Ni_{0.886}Co_{0.049}Mn_{0.050}Al_{0.015}]O_2$)

To prepare spherical NC-NCM $[Ni_{0.893}Co_{0.054}Mn_{0.053}](OH)_2$ precursor via co-precipitation, an aqueous solution of 2.0 M $NiSO_4{\cdot}6H_2O$ and $CoSO_4{\cdot}7H_2O$ (Ni:Co = 98:2, molar ratio) was used as the starting seed material for the core with a composition of $[Ni_{0.98}Co_{0.02}](OH)_2$. The solution was continuously fed into a batch reactor (17 L) filled with specific amounts of deionized water, NaOH (aq.), and NH_4OH (aq.) under an inert atmosphere (nitrogen gas). Simultaneously, NaOH (4.0 M, aq.) (molar ratio of sodium hydroxide to TM = 2.0) and a sufficient amount of NH_4OH (aq.) (molar ratio of ammonium hydroxide to TM = 1.2), as a chelating agent, were pumped into the reactor. During synthesis, the initially formed $[Ni_{0.98}Co_{0.02}](OH)_2$ particles became spherical under stirring. Then, to construct the NC-NCM structure, a Ni-deficient aqueous solution of 2.0 M $NiSO_4{\cdot}6H_2O$, $CoSO_4{\cdot}7H_2O$, and $MnSO_4{\cdot}H_2O$ (Ni:Co:Mn = 80:9:11, molar ratio), corresponding to the surface region composition of $[Ni_{0.80}Co_{0.09}Mn_{0.11}](OH)_2$, was introduced into the reactor. The obtained $[Ni_{0.893}Co_{0.054}Mn_{0.053}](OH)_2$ powder was filtered, washed, and dried under vacuum at 110 °C for 12 h. To prepare Li$[Ni_{0.886}Co_{0.049}Mn_{0.050}Al_{0.015}]O_2$, the precursor ($[Ni_{0.893}Co_{0.054}Mn_{0.053}](OH)_2$) was mixed with $LiOH{\cdot}H_2O$ and $Al(OH)_3{\cdot}3H_2O$ (Li:Al:(Ni + Co + Mn) = 1.01:0.015:0.985, molar ratio) and calcined at 730 °C for 10 h under an oxygen atmosphere.

Analytical techniques

The chemical compositions of the prepared powders were determined by inductively coupled plasma atomic emission spectroscopy (Optima 8300, PerkinElmer). Powder XRD (Empyrean, Panalytical) using Cu Kα radiation was used to identify the crystalline phases of the prepared powders. The XRD data were obtained in the 2θ range of 10–110° with a step size of 0.02°, and the collected XRD data were analyzed using the Rietveld refinement program FullProf. The particle morphologies and structures of all the powders were observed by SEM (Nova Nano SEM 450, FEI) and TEM (JEOL 2010, JEOL Ltd.). The TEM samples were prepared using a FIB, and element mapping was conducted using a JEOL JEM-ARM2100F (Cold FEG, JEOL Ltd) instrument. To confirm the localized composition of NCA90 and NCA-NCMA90, cross-sections of the particles were prepared by embedding the particles in an epoxy and grinding them flat. Line scans of the polished surfaces of the NCA90 and NCA-NCMA90 lithiated oxide were obtained via EPMA (Shimadzu, EPMA-1720).

Electrochemical testing

To fabricate the cathodes, the synthesized powders were mixed with carbon black and poly(vinylidene fluoride) (PVdF) (90:5.5:4.5, wt%) in *N*-methyl-2-pyrrolidone (NMP). The slurry was coated onto Al foil, vacuum dried, and roll-pressed. The electrolyte solution was 1.2 M $LiPF_6$ in ethylene carbonate–ethyl methyl carbonate (EC: EMC, 3:7 by vol%) with 2 wt% vinylene carbonate (VC). Preliminary cell tests were performed with

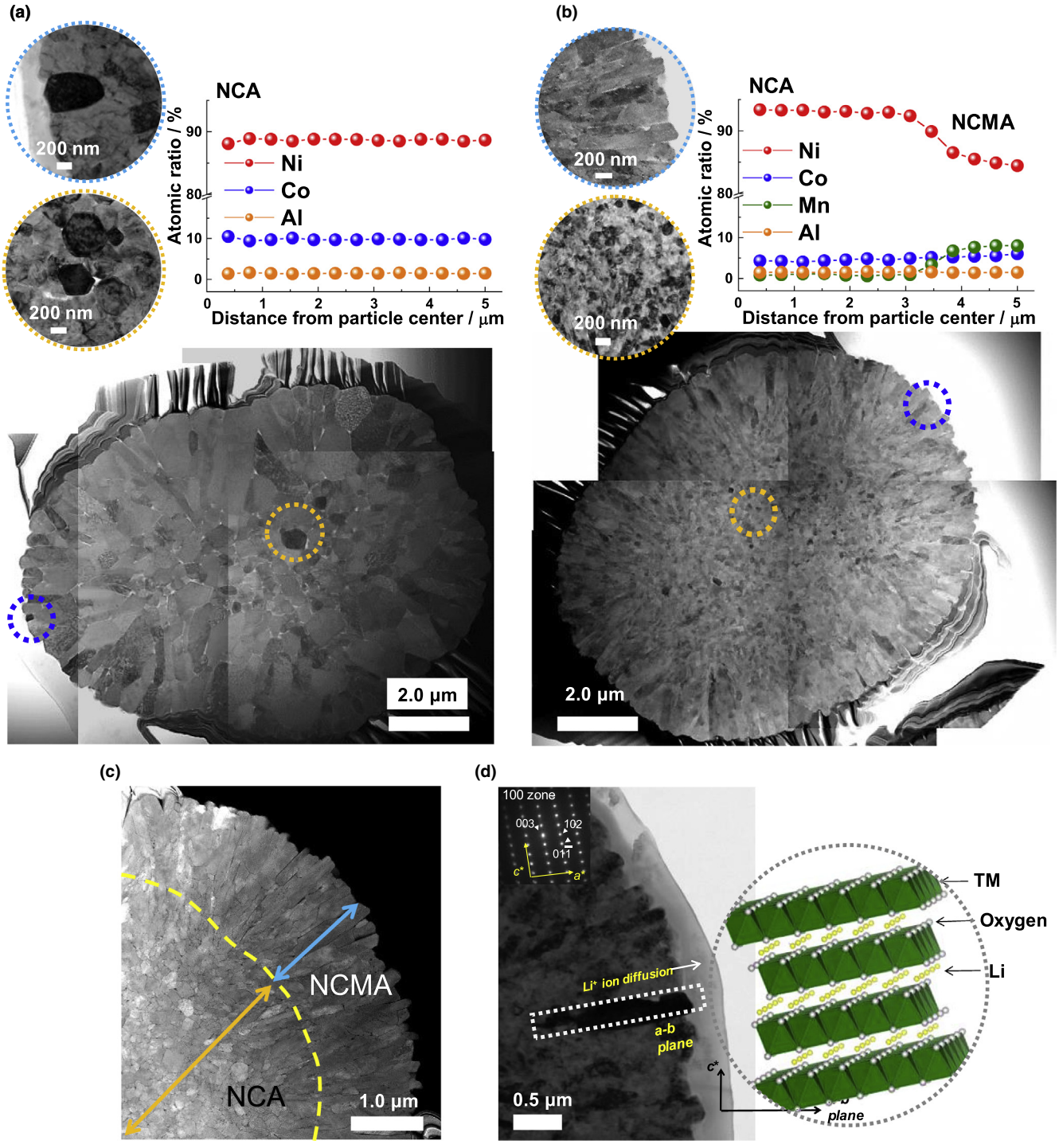

FIGURE 1

SEM, EPMA, and TEM results reveal the different microstructure of the NCA90 and NCA-NCMA90 cathode. Mosaic scanning TEM image of cross section cathode particle and EPMA composition profiles of (a) NCA90 and (b) NCA-NCMA90 cathode particle. Blue dash line indicated the particle center and orange dash line indicated particle core. The Ni-rich NCA particle center and the Mn-rich NCMA outer surface are clearly revealed by the EPMA line scans. (c) Dark field TEM image and (d) bright field TEM image of an NCA-NCMA90 primary particle with its corresponding electron diffraction pattern. The schematically shown crystallographic texture expedites the migration of lithium-ions toward the particle center.

2032 coin-type half-cells using lithium metal as the anode. The cells were charged and discharged by applying a constant current density of 90 mA g^{-1} at 0.5 C and 30 °C. Long-term cycle-life tests were performed in a laminated pouch-type full cell (28 mAh). MCMB graphite (Osaka Gas) was used as the anode. The cells were charged and discharged between 3.0 and 4.2 V by applying a constant 1 C current (30 mA corresponds to 200 mA g^{-1}) at 25 °C.

Results and discussion

Inductively coupled plasma atomic emission spectroscopy was used to determine the average compositions of the NCA90 and NCA-NCMA90 cathodes ($Li[Ni_{0.888}Co_{0.097}Al_{0.015}]O_2$ and $Li[Ni_{0.886}Co_{0.049}Mn_{0.050}Al_{0.015}]O_2$, respectively). Scanning electron microscopy (SEM) images of NCA90 and NCA-NCMA90 indicate that the particles in both cathodes are spherical with an average particle diameter of 9–10 μm and that each particle is composed of elongated primary particles with sizes of ~300 nm (Fig. S1). Rietveld refinement of the X-ray diffraction (XRD) data (Fig. S2) revealed that both cathodes have a rhombohedral layered structure (space group $R\bar{3}m$) without any impurity phases. The calculated lattice parameters suggest that the unit cell of NCA-NCMA90 was slightly expanded in both directions owing to the presence of Mn^{3+} (0.645 Å) and Ni^{2+} (0.69 Å), which have relatively large ionic radii.

Despite the similar chemical compositions, two widely different microstructural properties of the NCA90 and NCA-NCMA90 cathodes are demonstrated in Fig. 1a and b. Spatial elemental distributions measured across a sectioned particle using electron probe micro-analysis show that the concentrations of the transition metals in the NCA90 cathode were constant as expected. In comparison, the NCA-NCMA90 cathode contained well-defined concentration gradients at the interface region between the NCA core and the NCMA shell layer. The Ni, Co, Mn, and Al concentrations remained flat up to 3 μm from the particle center and then the Ni concentration decreased gradually from 92% to 84% at the NCA/NCMA interface, whereas the Mn concentration increased from 0.8% to 8.0%. Thus, the particle center mostly remained as a pure NCA cathode with a minimal amount of Mn. A comparison of the scanning transmission electron microscopy (STEM) images of NCA90 and NCA-NCMA90 cathode particles unequivocally shows the completely different internal microstructures of these two cathodes. The NCA90 cathode was composed of equi-axed primary particles that are ~0.5 μm in size. Both morphology and size of the primary particles at the particle core and near the particle surface were nearly identical. In contrast, the NCA-NCMA90 cathode exhibited a duplex microstructure in which the interior NCA region consisted of fine equiaxed primary particles and the NCMA shell region, which contains the Ni and Mn concentration gradients, was composed of mutually aligned elongated primary particles, similar to those typically observed in a full concentration gradient (FCG) NCM cathode [18,19,26,28,29]. The magnified STEM image of an NCA-NCMA90 particle in Fig. 1c clearly shows a demarcation line (marked by a dotted yellow line) that divides the rod-shaped primary particles, corresponding to the NCMA region, from the NCA region consisting of fine equiaxed primary particles, consistent with a cathode with a single uniform composition. The rod-shaped primary particles that are oriented radially in the NCMA

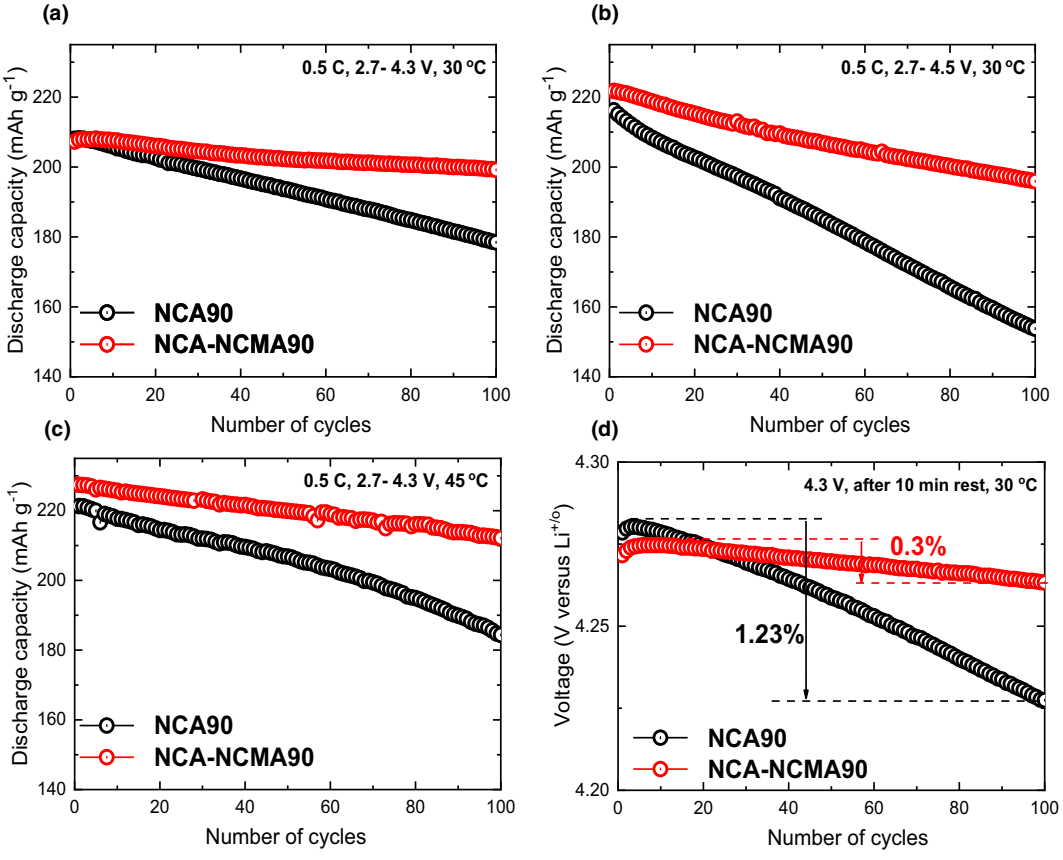

FIGURE 2

The NCA-NCMA90 cathode outperforms the conventional NCA90 cathode in terms of cycling stability. Cycling performance of the cathodes in the voltage ranges of (a) 2.7–4.3 V and (b) 2.7–4.5 V at 0.5 C and 30 °C in half-cells with a Li metal anode. (c) Cycling performance of the cathodes at 0.5 C and 45 °C. (d) OCV decays as a function of cycle number after charging at 4.3 V in (a).

region of the NCA-NCMA90 cathode have been proven to reduce the extent of parasitic side reactions between the cathode surface and the electrolyte and to partially relieve the internal strain arising from the anisotropic volume change during charging/discharging [18,26,28,30]. In addition to the observed particle morphology and spatial arrangement, which are conducive to stable cycling, the rod-shaped primary particles had a strong crystallographic texture, with the layer planes containing the Li ions aligned parallel to the radial direction of the secondary particles, as deduced from the [1 0 0] zone electron diffraction from the indicated primary particle at the periphery (Fig. 1d). Such crystallographically oriented primary particles along the radial direction should expedite Li migration toward the particle interior. The proposed NCA-NCMA90 hybrid cathode thus possesses all the advantages of an FCG cathode that have proven to be beneficial for cycling stability while incorporating both NCA and NCM compositions in a single cathode.

The fundamental electrochemical performance of the NCA90 and NCA-NCMA90 cathodes was characterized at different upper cut-off voltages (4.3 and 4.5 V) and also at an elevated temperature (45 °C) using a 2032 coin-type half-cell with a Li metal anode. Because of their nearly identical average compositions, the initial charge–discharge curves (at 0.1 C and 30 °C) in Fig. S3 show that NCA90 and NCA-NCMA90 cathodes produced similar discharge capacities of approximately 222 and 225 mAh g^{-1}, respectively, at 4.3 V (Fig. S3a, first-cycle Coulombic efficiency = ~95%) and up to 236 mAh g^{-1} at 4.5 V (Fig. S3b) for the NCA-NCMA90 cathode. Despite the hybrid structure of NCA-NCMA90, its initial charge–discharge curves exhibited voltage profiles nearly identical to those of the NCA90 cathode. The cycling performances, however, were markedly different. After 100 cycles, the NCA90 cathode cycled retained 87.6% of the initial capacity when cycled at 4.3 V (at 0.5 C) and only 71.1% when cycled at 4.5 V. In comparison, the NCA-NCMA90 cathode maintained 96.1% of the initial capacity at 4.3 V (Fig. 2a) and 88.3% at 4.5 V over the same cycling period (Fig. 2b). The NCA-NCMA90 cathode also outperformed the NCA90 cathode at 45 °C, as the capacity retention for the NCA-NCMA90 cathode exceeded 93% when cycled at 4.3 V, whereas that of the NCA90 cathode was limited to 83.3% (Fig. 2c). Thus, the NCA-NCMA90 cathode was able to deliver a higher capacity with a significant reduction in capacity fading, even at a higher potential (4.5 V) and higher temperature (45 °C). As expected from the better cycling stability during repeated charge–discharge, the NCA-NCMA90 cathode shows a stable Coulombic efficiency with reduced fluctuation and the Coulombic efficiency of the NCA-NCMA90 cathode stabilizes faster during its initial cycles compared to the NCA90 cathode (Fig. S4). In addition, the NCA-NCMA90 cathode shows excellent rate capability up to 2 C rate with capacity retention of 79 % (vs. the capacity at 0.2 C; this value is highly compatible to the commercialized the $Li[Ni_{0.6}Co_{0.2}Mn_{0.2}]O_2$, $Li[Ni_{0.8}Co_{0.1}Mn_{0.1}]O_2$, and $Li[Ni_{0.8}Co_{0.16}Al_{0.04}]O_2$ [4,12] cathodes, showing enough acceptability for practical application (Fig. S5). Fig. 2d presents the open-circuit voltages (OCVs) of the half-cells measured at the charge end state (4.3 V) after 10 min of relaxation as a function of the cycle number. In the case of NCA90, the OCV continuously decayed, such that the initial OCV was reduced by 1.2% after 100 cycles. In contrast, the OCV of the NCA-NCMA90 cathode decreased by only 0.3%. The drop in the OCV, which represents an intrinsic chemical driving force for Li extraction, is most likely caused by structural degradation of the cathode arising from the H2 → H3 phase transition, as it has also been shown that electrochemically delithiated $Li[Ni_{0.933}Co_{0.031}Al_{0.036}]O_2$ and $LiNiO_2$ undergo a continuous H2 → H3 phase transformation during relaxation from the deeply charged state [31]. The dQ dV^{-1} curves of the materials clearly show all the phase transition relevant to both NCA90 and NCA-NCMA90 cathodes (Fig. S6).

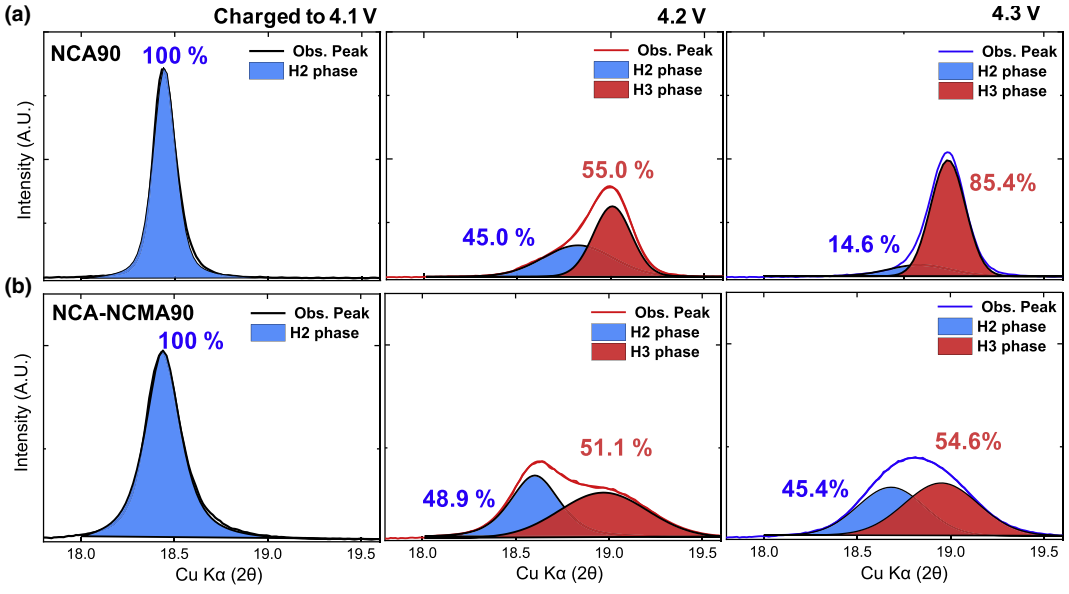

FIGURE 3

Ex situ XRD patterns during the first cycle attest to the structural stability of the NCA-NCMA90 cathode. Fraction of H2 and H3 phases estimated from the (0 0 3) reflections of different first-charge states (4.1, 4.2, and 4.3 V) for the (a) NCA90 and (b) NCA-NCMA90 cathodes.

Judging by the relative intensities of the H2 → H3 phase transition peaks in the dQ dV^{-1} profiles for the NCA90 and NCA-NCMA90 cathodes, however, the extent of the detrimental phase transition was substantially suppressed for the NCA-NCMA90 cathode, despite its similar Ni content. Moreover, the H2 → H3 phase transition peak for the NCA-NCMA90 cathode hardly changed during cycling whereas that of the NCA90 cathodes gradually decayed, indicating that the initial structure was not fully recovered but continuously deteriorated during cycling. The extent of the OCV drop and the dQ dV^{-1} curves suggest that the phase transition, which is detrimental to the structural integrity owing to anisotropic volume contraction and its abrupt nature [10,13,32–34], was retarded by the hybrid structure of the NCA-NCMA90 cathode.

To study the extent of the H2 → H3 phase transition explicitly, ex situ XRD measurements of the two cathodes were performed as a function of the state of charge (4.1, 4.2, and 4.3 V). Fig. 3a and 3b shows the (0 0 3) XRD reflections for the two cathodes. Both cathodes were fully transformed to the H2 phase at 4.1 V, after which the H3 phase began to appear as a shoulder superimposed on the (0 0 3) reflection of the H2 phase. Using the relative peak intensities of the deconvoluted (0 0 3) reflections for the H2 and H3 phases, the weight fraction of each phase was determined to be approximately 50%. When charged to 4.3 V, the NCA90 cathode was nearly completely converted to the H3 phase, whereas the NCA-NCMA90 cathode retained a substantial fraction of the H2 phase. The ex situ XRD data unequivocally demonstrate that the conversion to the H3 phase was considerably retarded in the case of the NCA-NCMA90 cathode, resulting in the suppression of sudden unit cell contraction in the *c*-direction (average lattice parameter change on charging from 4.1 to 4.3 V, $\Delta c = -4.64\%$ for NCA90 and -2.96% for NCA-NCMA90). The lattice contraction was highly anisotropic because the *a*-axis lattice parameter remained relatively constant during charging from 4.1 to 4.3 V (Figs. 3, S7, and Table S1). This anisotropic unit cell contraction led to localized stress concentrations, causing the nucleation of microcracks along the interparticle boundaries and undermining the overall mechanical integrity of the cathode particles [10,13,33–35]. Hence, the retardation of H3 formation exhibited by the NCA-NCMA90 cathode is beneficial for maintaining its structural stability, as clearly revealed by SEM images of the cross-sections of NCA90 and NCA-NCMA90 particles charged to 4.3 V (Fig. S8). Microcracks initiated from the particle center and propagated to the surface are clearly visible in each charged NCA90 cathode particle. The repeated opening and closing of such microcracks will eventually pulverize the cathode particles, as shown later. Moreover, the microcracks also provide pathways for electrolyte infiltration into the particle

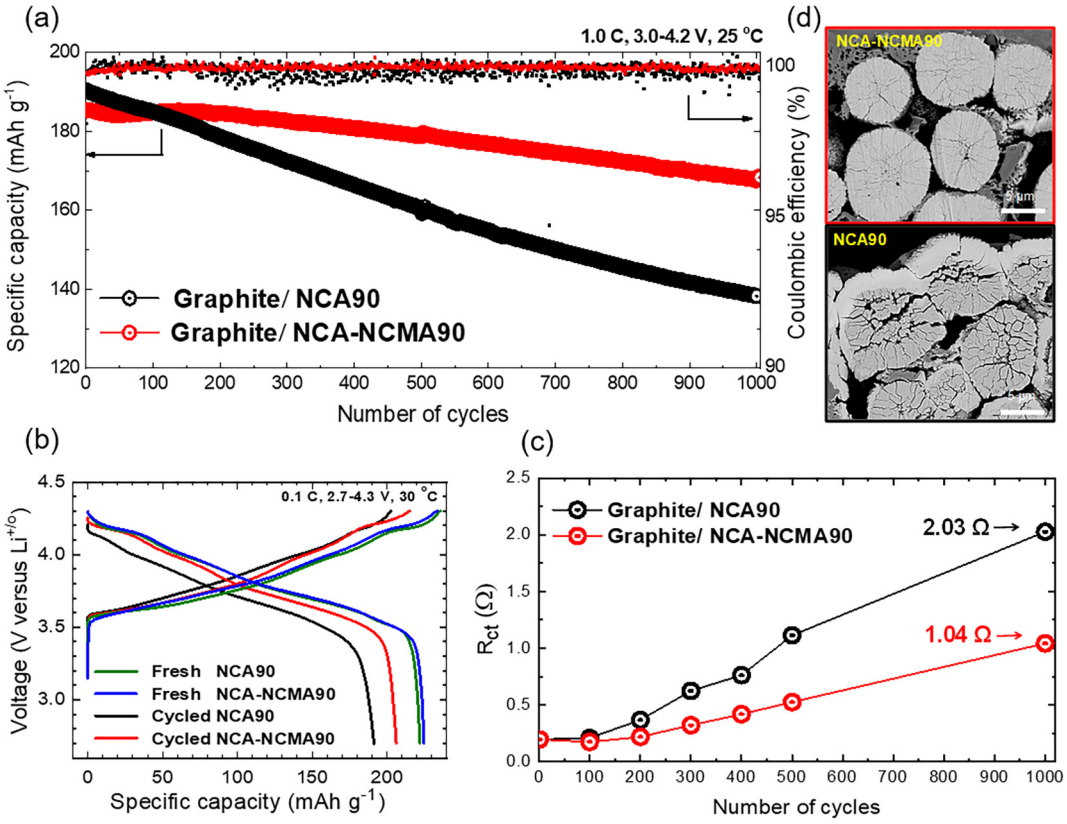

FIGURE 4

Comparison of long-term cycling, impedance measurements as a function of cycle number, and SEM images after 1000 cycles for NCA90 and NCA-NCMA90. (a) Long-term cycling performance of the NCA90 and NCA-NCMA90 cathodes in full cells. (b) First-cycle voltage profiles of the NCA90 and NCA-NCMA90 cathodes recovered after 1000 cycles. The half-cells were reassembled using a fresh Li metal anode and fresh electrolyte to examine the degradation of the cycled cathodes and anode (Fig. S3 and S10). (c) Charge transfer resistance of the NCA90 and NCA-NCMA90 cathodes estimated from the Nyquist plots as a function of the number of cycles in Fig. S11. Cross-sectional SEM images of the (d) NCA90 and NCA-NCMA90 cathodes from the full cells after 1000 cycles.

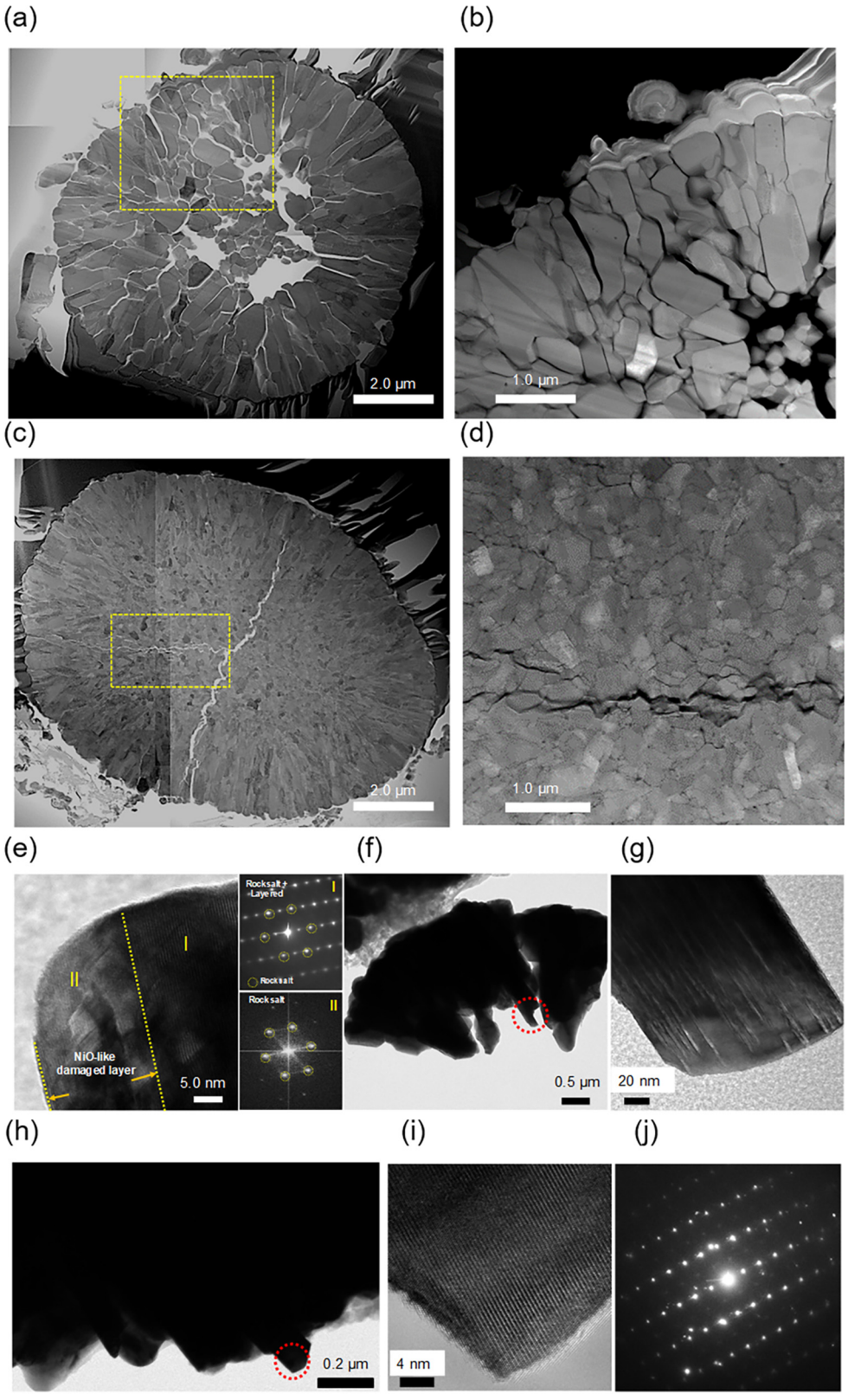

FIGURE 5

Visual image of the cycled NCA-NCMA90 cathode verifies its mechanical and structural stability. (a) Mosaic scanning TEM image of the cycled NCA90 electrode after 1000 cycles. (b) Magnified image of the area marked by the yellow box in (a). (c) Mosaic scanning TEM image of the cycled NCA-NCMA90 cathode after 1000 cycles. (d) Magnified image of the area marked by the yellow box in (c). (e) High-magnification TEM image of the surface and FT images of the marked regions. (f) Bright-field TEM image of the fractured NCA90 cathode after 1000 cycles. (g) High-resolution TEM image of the marked area in (f) showing the material loss incurred during cycling. (h) Bright-field TEM image near the surface of the cycled NCA-NCMA90 cathode. (i) High-resolution TEM image and (j) corresponding electron diffraction pattern from a surface primary particle of the cycled NCA-NCMA90 cathode.

interior and accelerate the surface degradation of the crack faces, forming impedance-increasing internal resistive surfaces. In contrast, the NCA-NCMA90 cathode particles were strikingly unaffected by the extraction of Li ions, as an appreciable network of microcracks did not develop the charge end state, similar to the retardation of the detrimental H2 → H3 phase transition previously observed in FCG cathodes [28]. In addition, the unique geometrical arrangement of the primary particles—a highly ordered orientation of the elongated primary particles combined with a strong crystallographic texture—observed in FCG cathodes helped to relieve the internal strain arising from H3 anisotropic contraction. Because the volume contraction is confined to the *c*-direction (i.e., the radial direction), the internal strain from the H3 phase transition is evenly distributed in the NCA-NCMA90 cathode and the secondary particles can uniformly contract without local stress build-up. The elongated particle shape also favors deflection of any shear stress caused by the H3 phase transition. A numerical analysis of the stress–strain behavior of packings of elongated particles demonstrated that the shear strength of the particle packing was a linearly increasing function of the elongation because of the increased contact area [36]. It was also noted that the nano-sized primary particles in the interior of the NCA-NCMA90 cathode particles (Fig. 1b) also contributed to suppressing the nucleation of microcracks and inhibiting their subsequent propagation because the numerous grain boundaries acted as effective barriers for crack propagation. The stated advantages of the NCA-NCMA90 microstructure all contributed to negating the deleterious effect of the H3 phase transition, thus greatly improving the cathode cycling stability.

To demonstrate sustained capacity retention with extended cycling and hence the feasibility of the hybrid cathode design for practical applications, the two cathodes were compared in pouch-type full cells using commercial mesocarbon microbead (MCMB) graphite as the anode for long-term cycling and for post-mortem analysis. The MCMB graphite anode used in the pouch-type full-cell testing displayed typical structural properties and electrochemical performances in Li half cells (in Fig. S9). The initial capacities (196 mAh g^{-1} at 0.1 C) of the two cathodes were nearly identical owing to their similar average compositions, as seen in the half-cells. However, the Mn contained in the NCMA layer and its rod-shaped primary particles had a clear effect, as the NCA-NCMA90 cathode displayed a superior capacity retention of 90.5% after 1000 cycles when cycled between 3.0 and 4.2 V at 1.0 C, whereas the NCA90 cathode retained only 60.2% of its initial capacity (Fig. 4a). To the best of our knowledge, the capacity retention achieved by the NCA-NCMA90 cathode over 1000 cycles using 100% depth of discharge (DOD) is the highest capacity retention for a pouch-type full cell using an NCA cathode with a Ni content greater than 90%. A Ni-rich NCA cathode did maintain 80% of its initial capacity after 2000 cycles, but only when the available DOD was limited to 60% [37].

To further substantiate the superior cycling stability of the NCA-NCMA90 cathode, the cycled full cells were disassembled to recover the cathodes and anodes. To determine the relative extent of degradation sustained during long-term cycling, each electrode was reassembled in a half-cell with a Li metal anode. The anodes recovered from the NCA90 and NCA-NCMA90 full cells nearly reproduced the specific capacities of uncycled fresh anodes (Fig. S10), in agreement with previous results for long-term cycling of Ni-rich NCM cathodes [37]. The first-cycle discharge capacities of the recovered NCA90 and NCA-NCMA90 cathodes were reduced by 14% (191 mAh g^{-1}) and by 8% (206 mAh g^{-1}), respectively, relative to the capacities of the corresponding fresh cathodes (Fig. 4b). The full-cell capacity fading was most likely caused by the cathode degradation. It is also interesting that the recovered NCA cathode was able to deliver 86% of the capacity produced by the fresh cathode, whereas the corresponding full cell lost 40% of the initial capacity over 1000 cycles. This finding suggests that the cathode degradation accelerates electrolyte consumption, leading to further capacity loss. Therefore, using a stable cathode, such as NCA-NCMA90, helps to preserve the electrolyte during long-term cycling.

The stability of the NCA-NCMA90 cathode was also demonstrated by the charge transfer resistances, R_{ct}, estimated from the electrochemical impedances measured at intermittent intervals during 1000 cycling (Fig. 4c, Fig. S11). The surface structure degradation compounded by the electrolyte consumption led to a continuous build-up of an impedance-increasing surface film, as R_{ct} for both cathodes increased almost linearly with the cycle number; however, the R_{ct} value of the NCA90 cathode after 1000 cycles (2.03 Ω) was twice as large as that of the NCA-NCMA90 cathode. The Ni-deficient and Mn-rich surface composition together with the minimization of electrolyte infiltration through microcracks helped to suppress the impedance increase at the particle surface.

SEM images of the cycled particles and their cross-sections reveal the relative extent of the structural damage sustained during cycling. A substantial fraction of the cycled NCA90 particles was severely fractured, with some particles nearly pulverized (Fig. 4d). The cross-sectional image indicates that even the particles that appeared to remain intact contained numerous microcracks that traversed the entire particle, nearly fracturing the particle into several pieces. In comparison, the original spherical morphology of the NCA-NCMA90 particles was well maintained following cycling, and the observed cracks were mostly arrested before reaching the surface, confirming the structural stability of the NCA-NCMA90 cathode (Fig. 4d). The structural damage incurred by each cathode during cycling was also assessed by examining the cycled cathodes using TEM. In the case of the cycled NCA90 cathode, because most of the particles were nearly pulverized, an intact particle was deliberately chosen for focused ion beam (FIB) sample preparation (Fig. 5a). The bright-field STEM image of the cycled NCA90 cathode shows numerous microcracks emanating from the particle center and reaching the surface along the particle boundaries, confirming that even NCA90 cathode particles that appeared to remain intact sustained serious mechanical damage. Fig. 5b displays a magnified dark-field STEM image of the microcracks, which form bridges between the voids in the particle core and the surface, allowing electrolyte penetration into the particle interior. In comparison, very few microcracks were observed in the cycled NCA-NCMA90 cathode (Fig. 5c). The vertical crack traversing the entire particle likely formed during electrode preparation (roll pressing), as the crack appears to have been initiated from the bottom surface, not from the particle center. The nano-sized primary particles deflected a crack that was initiated from the

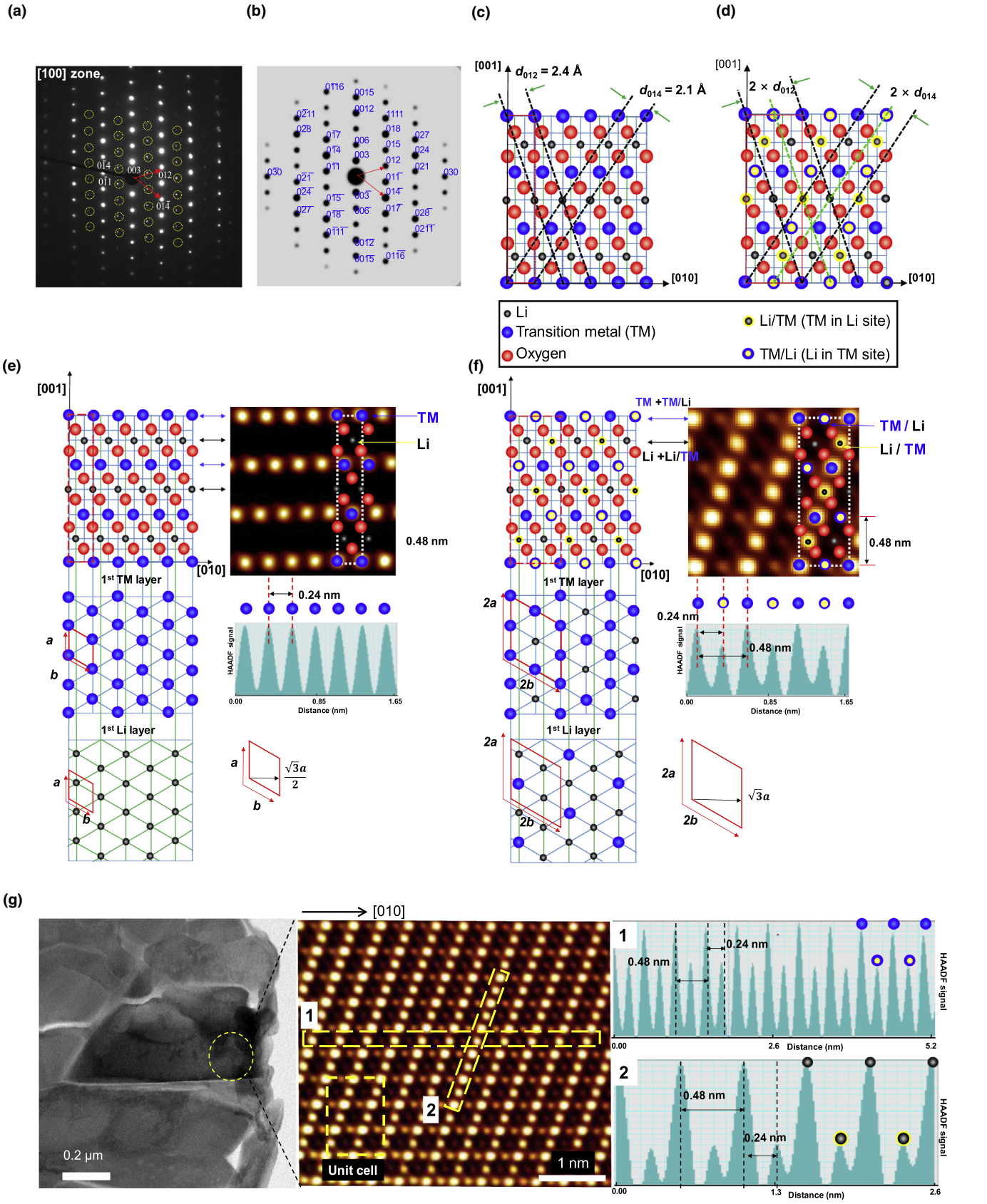

FIGURE 6

A new type of cation (Li/TM) ordering revealed. (a) SAED pattern from a primary particle at the periphery of the cycled NCA-NCMA90 cathode. (b) Calculated [1 0 0] zone diffraction pattern of a normal layered structure ($R\bar{3}m$). Structure projected in the [1 0 0] direction: (c) normal layered structure and (d) cation (Li/TM) ordered layered structure. HAADF TEM images and schematic diagrams of the (e) normal and (f) cation-ordered (Li/TM) structure. (g) TEM and HAADF images of the cation-ordered structure with line scans of the atomic columns along the [0 0 1] and [0 1 2] directions.

particle center, resulting in a zigzag path and finally arresting its propagation before reaching the surface (Fig. 5d). The images shown in Fig. 5a–d clearly demonstrate the markedly different microstructures of the NCA90 and NCA-NCMA90 cathodes that resulted in strikingly different responses to the mechanical stress associated with Li extraction and insertion.

To assess the surface damage caused by electrolyte attack, the cycled cathodes were also examined using TEM without any treatments to minimize the distortion of the surface structure during TEM sample preparation. As expected from the observed capacity fading, the cycled NCA90 cathode incurred extensive surface damage in the form of a thick NiO-like layer (~15 nm), as shown in Fig. 5e and accompanying Fourier transform (FT) images of the surface and subsurface regions (inset, Fig. 5e) clearly reveal the transformation of the surface structure. This transformation is similar to that frequently observed on the surfaces of cycled Ni-rich layered cathodes, which is recognized as a leading cause of increased charge resistance during cycling. A fractured NCA90 cathode particle (Fig. 5f) was selected to examine the interior primary particles that were exposed to the infiltrated electrolyte. The TEM image of such a primary particle (Fig. 5g) shows thin strips where material has been dissolved away. Hence, in addition to surface damage, the interior primary particles of the cycled NCA90 cathode also sustained severe material loss. In comparison, the pristine surface of the NCA-NCMA90 cathode was remarkably well preserved (Fig. 5h–j). The TEM image of a primary particle on the surface of the cycled NCA-NCMA90 cathode reveals that the layered structure was preserved to the very edge of the primary particle, which was covered by ~5 nm-thick NiO-like layer, as a result of successful compositional and structural engineering of the particle surface.

Moreover, one of the striking structural features observed in the cycled NCA-NCMA90 cathode (after 1000 cycles) was the ordering of cations in both the TM and Li planes in the layered structure, which was observed previously by our group in a Zr-doped $LiNiO_2$ cathode [27]. The selected area electron diffraction (SAED) pattern from a primary particle at the periphery of the cycled NCA-NCMA90 cathode oriented along the [1 0 0] direction (Fig. 6a) not only shows strong diffraction spots corresponding to the normal layered structure (cf. calculated [1 0 0] zone diffraction pattern of a layered structure, such as $LiCoO_2$ or $LiNiO_2$ in Fig. 6b), but also contains extra peaks at a ½ spacing (circled in yellow in Fig. 6a). Two diffraction vectors, 0 1 2 and 0 1 $\bar{4}$ are labeled in Fig. 6a, and the corresponding lattice planes drawn on the lattice of the normal layered structure projected in the [1 0 0] direction are shown in Fig. 6c. The extra peaks at the half spacing of the 0 1 2 and 0 1 $\bar{4}$ vectors, 0 ½ 1 and 0 ½ $\bar{4}$, translate to a periodicity with spacings that are twice those of the 0 1 2 and 0 1 $\bar{2}$ vectors in the structure, thus necessitating the existence of a superlattice. One possible structural solution for the superlattice is the ordered occupation of Li ions in the TM layer and TM ions in the Li layer, as sketched in Fig. 6d. In this atomic configuration, all the extra diffraction spots, including 0 ½ 1 and 0 ½ $\bar{2}$, can be explained as indicated in Fig. 6d. A similar diffraction pattern with extra peaks found for highly delithiated $Li_{0.63}Ni_{1.02}O_2$ was interpreted as Li/vacancy ordering in the Li layer, which maintained the rhombohedral lattice of $LiNiO_2$ ($R\bar{3}m$) but had cell parameters twice as long as those of $LiNiO_2$ [38]. Although cation ordering of the TM ions in a TM layer is often observed, as in $LiNi_{0.5}Mn_{0.5}O_2$ [39], to the best of our knowledge, Li/TM ordering in a layered NCM or NCA cathode has not been reported to date.

To verify the Li/TM ordering unequivocally, high-angle annular dark field (HAADF) imaging was used to image the ordered lattice structure of the cycled NCA-NCMA90 cathode directly. As illustrated in Fig. 6e, in a TEM image of the normal layered structure with fully occupied Li and Ni layers, a string of Ni atoms with equal contrast can be resolved, whereas Li atoms are rarely visible because of their low scattering contrast. In the Li/TM ordered lattice in Fig. 6f, Li ions occupy half of the TM sites in every other column of TM ions in the TM layer and vice versa in the Li layer, creating a superstructure unit cell. This alternating occupation of Li ions in the TM layer produces a regular oscillation in the contrast of the TM layer because half of the TM ions in every other TM row are replaced by Li ions, which have a much lower atomic number (hence, the low contrast). The corresponding experimental HAADF image clearly duplicates the alternating nature of the TM layer, as confirmed by the line scan across the TM layer, which exhibits a regular oscillation in the contrast with a periodicity of $\sqrt{3}a$. The oscillating contrast was also observed in the Li layer owing to the regular replacement of Li sites by heavier TM ions. Fig. 6g shows a bright-field TEM image of the primary particle from which the SAED pattern was obtained, revealing that Li/TM ordering was obtained. Because the SAED aperture covers an area that is as large as 100 nm in diameter, the Li/TM ordering is not a localized phenomenon, but extends several hundreds of nanometers. Identical SAED patterns were observed in many primary particles (Fig. S12), indicating that the Li/TM ordering is a general microstructural feature developed during cycling of the NCA-NCMA90 cathode. The vertical and horizontal line scans of the atomic columns and rows in the [1 0 0] zone HAADF image in Fig. 6g verify the oscillating contrast and the periodicity is well matched to the structure inferred from the SAED pattern. We believe that the Li/TM ordering is a unique microstructural attribute of the NCMA encapsulating layer developed during cycling. Further, this phenomenon protects the particle surface from structural degradation, as observed in Fig. 5. Moreover, an appropriate level of cation ordering can be beneficial by reducing its voltage decay and/or capacity fade during extensive cycling observed in Fig. 2. Density functional theory calculations have been used to verify that the Li/Ni ordering in Zr-doped $LiNiO_2$ is energetically favorable and, moreover, lowers the energy required to extract Li ions from the host material [27]. Hence, it is likely that the Al doping of the highly Ni-enriched NCA cathode promoted the observed Li/TM ordering during repeated extraction and insertion of Li ions, facilitating Li intercalation and stabilizing the structure during extended cycling of the NCA-NCMA90 cathode.

Conclusion

The proposed NCA-NCMA90 cathode represents a truly hybrid cathode material, that is compositionally and microstructurally engineered to achieve a performance standard that easily surpasses the currently available LIB cathodes in terms of both energy density and cycling stability. The NCA-NCMA90 cathode,

which was highly enriched in Ni to provide a high discharge capacity, combined the NCA and NCM cathodes within a single particle resulting in microstructural attributes that improved its cycling stability. Specifically, the spatially correlated peripheral primary particles were crystallographically textured, which expedited Li intercalation, and the nano-sized core primary particles deflected and inhibited the propagation of the microcracks produced by inherent anisotropic volume changes of the cathode during charging/discharging. In addition, we observed Li/TM cation ordering in the NCA-NCMA90 cathode on a microscopic scale, which likely stabilized the host structure during cycling and facilitated Li intercalation. We believe that the novelty of the proposed cathode lies in the use of a quaternary layered cathode consisting of Ni, Co, Mn, and Al as a shell material, while the core is composed of a well-tested NCA cathode. This combination of materials has not been tried previously and provides optimal structural and electrochemical properties that outperform the layered cathodes reported in the literature (Fig. S13 and Table S2). Moreover, we provided evidence for a new type of cation ordering comprising of Li and transition metals that have not been previously reported in a Ni-rich NCM cathode. LIBs based on the proposed cathode will be able to provide a new generation of EVs with a sufficient driving range at a lower cost and with a longer life, making general electromobility one step closer to reality.

Acknowledgments

This work was mainly supported by the Global Frontier R&D Program (2013M3A6B1078875) of the Center for Hybrid Interface Materials (HIM) funded by the Ministry of Science, Information & Communication Technology (ICT) and by a National Research Foundation of Korea (NRF) grant funded by the Korea government Ministry of Education and Science Technology (MEST) (NRF-2018R1A2B3008794).

Author contributions

Y.-K.S. supervised the project. Y.-K.S. and C.S.Y. designed the experiments. J.-H.K. and U.-H.K. synthesized the cathode and tested the cathode and anode. C.S.Y. and U.-H.K. contributed to analyze the TEM imaging experiments. J.-Y.H. performed and analyzed cross-section polishing. C.S.Y. and Y.-K.S., wrote the paper. H.H.R. performed and analyzed the X-ray measurements. All of the authors contributed to the discussion section and the finalization of the text and Figures of manuscript.

Competing financial interests

The authors declare no competing financial interests.

Appendix A. Supplementary data

Supplementary data to this article can be found online at https://doi.org/10.1016/j.mattod.2018.12.004.

References

[1] J.B. Goodenough, K.-S. Park, J. Am. Chem. Soc. 135 (2013) 1167–1176.
[2] J.M. Tarascon, M. Armand, Nature 414 (2001) 359–367.
[3] U.S. Department of Energy, Annual Merit Review – Energy storage technologies. https://www.energy.gov, 2012.
[4] S.-T. Myung et al., ACS Energy Lett. 2 (2017) 196–223.
[5] 21st Asia and South Pacific Design Automation Conference (ASP-DAC), Macau, January 25–28, 2016.
[6] Y. Zhou, T. Stephens, E-Drive vehicle sales analyses: Vehicle technologies annual merit review; Project VAN011; Argonne National Laboratory, 2014.
[7] Zhitong Xiao et al., Sci. Bull. 63 (2017) 46–53.
[8] Luoluo Wang et al., Sci. China Mater. 59 (2016) 95–103.
[9] https://www.tesla.com, accessed July, 2018.
[10] H.-H. Ryu et al., Chem. Mater. 30 (2018) 1155–1163.
[11] C.S. Yoon et al., J. Electrochem. Soc. 162 (2015) 2483–2489.
[12] H.-J. Noh et al., J. Power Sources 233 (2013) 121–130.
[13] L. Biasi et al., Phys. Chem. 121 (2017) 3286–3294.
[14] S.-M. Bak et al., ACS Appl. Mater. Interfaces 6 (2014) 22594–22601.
[15] S. Hwang et al., Chem. Mater. 27 (2015) 3927–3935.
[16] Y.-K. Sun et al., Phys. Chem. B 110 (2006) 6810–6815.
[17] Y.-K. Sun et al., Nat. Mater. 8 (2009) 320–324.
[18] H.-J. Noh et al., Chem. Mater. 25 (2013) 2109–2115.
[19] B.-B. Lim et al., Adv. Funct. Mater. 25 (2015) 4673–4680.
[20] D.-W. Jun et al., Chem. Mater. 29 (2017) 5048–5052.
[21] J. Shim et al., J. Power Sources 112 (2002) 222–230.
[22] K.A. Striebel et al., J. Electrochem. Soc. 151 (2004) 857–866.
[23] F. Zhou et al., Electrochem. Solid-State Lett. 12 (2009) 81–83.
[24] S.-W. Woo et al., Electrochim. Acta 54 (2009) 3851–3856.
[25] T.E. Conry et al., Chem. Mater. 24 (2012) 3307–3317.
[26] U.-H. Kim et al., Adv. Energy Mater. 6 (2016) 1601417.
[27] C.S. Yoon et al., Chem. Mater. 30 (2018) 1808–1814.
[28] C.S. Yoon et al., Chem. Mater. 29 (2017) 10436–10445.
[29] C.S. Yoon et al., Adv. Funct. Mater. 28 (2018) 1802090.
[30] J.H. Lee et al., Energy Environ. Sci. 9 (2016) 2152–2158.
[31] A. Tamura et al., Electrochem. Soc. 164 (2017) 1514–1519.
[32] H. Liu et al., Nano Lett. 17 (2017) 3452–3457.
[33] C.S. Yoon et al., ACS Energy Lett. 2 (2017) 1150–1155.
[34] J.-M. Lim et al., Sci. Rep. 7 (2017) 39669.
[35] C.S. Yoon et al., J. Mater. Chem. A 6 (2018) 4126–4132.
[36] E. Azéma, F. Radjaï, Phys. Rev. E 81 (2010) 051304.
[37] S. Watanabe et al., J. Power Sources 260 (2014) 50–56.
[38] J.P. Peres, F. Weill, C. Delmas, Solid State Ionics 116 (1999) 19–27.
[39] Y.S. Meng et al., Chem. Mater. 17 (2005) 2386–2394.